IET Radar, Sonar & Navigation

WILEY

The Institution of Engineering and Technology

ORIGINAL RESEARCH OPEN ACCESS

Polarimetry for Sparse Multistatic 3D SAR

Richard Welsh[1] | Daniel Andre[1] | Mark Finnis[2]

[1]Centre for Electronic Warfare, Information and Cyber, Cranfield University, Defence Academy of the United Kingdom, Shrivenham, UK | [2]Centre for Defence Engineering, Cranfield University, Defence Academy of the United Kingdom, Shrivenham, UK

Correspondence: Richard Welsh (Richard.Welsh@cranfield.ac.uk)

Received: 7 February 2025 | **Revised:** 6 March 2025 | **Accepted:** 17 March 2025

Handling Editor: Hugh Griffiths

Funding: This study was funded by Dstl.

Keywords: multistatic radar | radar interferometry | radar polarimetry | synthetic aperture radar

ABSTRACT

There is significant interest in multistatic SAR image formation, due to the increased development of satellite constellations and UAV swarms for remote sensing applications. The exploitation of the finer resolution and wider coverage of these geometries has been shown to reduce the often-impractical data collection requirements of 3D SAR imagery; this offers advantages such as improved target identification and the removal of layover artefacts. This paper presents a novel polarimetric generalisation of the SSARVI algorithm, which was previously developed to exploit sparse aperture multistatic collections for 3D SAR image formation. The new algorithm presented here, named the PolSSARVI algorithm, combines polarimetrically weighted interferograms for determining the 3D scatterer locations from sparse aperture polarimetric collections. The bistatic generalised Huynen fork polarimetric parameters are then determined for the multistatic PolSSARVI 3D SAR renderings. This new approach was tested on both simulated and experimental data. Experimental imagery was formed using measurements from the Cranfield GBSAR laboratory.

1 | Introduction

When compared to a conventional monostatic synthetic aperture radar (SAR), multistatic SAR image formation can be used to improve the resolution and coverage of SAR systems and capture additional target information from multiple aspect angles [1, 2]. This has led to increased interest in SAR missions employing satellite constellations and UAV-SAR drone swarms [3, 4]. The advantages of multistatic SAR could be exploited for 3D imaging scenarios, which often have impractically high sampling requirements [5]. Moreover, multiple aspect angle collections make multistatic geometries beneficial for capturing additional target scattering information, including polarimetric [6].

3D SAR has the benefit of separating target features overlaid in height and thus removing layover distortions from imagery. However, producing sufficient resolution and coverage in the vertical direction conventionally requires many repeat passes over multiple aperture heights with Nyquist sampled spacing [7, 8]. With conventional 3D SAR imaging algorithms, a reduction in the number of passes can make the collection more realisable, and, however, would reduce image quality with aliasing ambiguities.

Various techniques have been developed for reducing the sampling requirements of 3D SAR while maintaining image quality, and these include differential SAR interferometry, 3D SAR compressive sensing and the SAR point-cloud generation

system (SPCGS) [9–11]. SAR interferometry relies on a phase unwrapping process to generate scatterer height estimates [12] and has primarily seen success with digital elevation mapping. However, the phase unwrapping step can introduce ambiguities for scenes with large discontinuities in their height profile [11]. 3D SAR compressive sensing has seen significant interest, with renderings of complex vehicle targets being successfully produced [13]. This approach requires the target scene to be sparsely populated, which is then exploited in the signal reconstruction. The approach can be computationally expensive [14]. However, recently introduced methods based on sparse-prior optimisation are attempting to improve this [15].

The SPCGS algorithm processes the change in layover within a stack of 2D SAR images obtained from different radar platform trajectory heights and sums the interferometric contribution to generate sparse scatterer height estimates [10, 16]. This can be challenging for bistatic, multistatic SAR geometries and even more so for SAR near-field geometries where the elevation angle across the scene is spatially variant. Under these conditions, the layover position of scatterers is difficult to calculate due to significant distortions of the contributing SAR iso-range arcs (constant range contours) [17]. The sparse SAR volumetric interferometry (SSARVI) approach was developed to overcome this [18, 19].

This paper contributes a new polarimetric generalisation of the multistatic SSARVI algorithm, which we denote PolSSARVI. The PolSSARVI algorithm utilises the novel volumetric interferometry-based approach, developed in the previous SSARVI literature, to account for the layover distortions attributed to using multistatic and near-field SAR collections. This paper extends the capability of this approach further by combining multiple volumetric interferograms for each measured polarisation channel for a sparsely sampled 2D multistatic aperture. The polarimetric interferograms are each weighted by their combined polarimetric span intensity. This combined polarimetric approach was devised to better account for the variability of scatterer brightness in different polarisation channels and enable the association of polarimetric information with 3D scatterer detections. Examples of such scatterers, including a discussion on polarimetric scattering variability, can be found here [20]. The new methodology introduced by the PolSSARVI algorithm is explained in greater detail in Section 2.

Previous studies of the SSARVI algorithm were based on the overlay of individual polarisation channel detections, which although contributing more detections did not provide polarimetric scatterer properties [19]. The polarimetric information determined for the 3D targets presented in this study is obtained from bistatic Huynen fork parameters, which were developed from the pioneering work of Huynen and later Titin-Schnaider [21–24]. The development of these parameters is explained in more detail in Section 3.

Recent studies highlight the utility of extending SAR imaging techniques to include polarimetric analyses, particularly for improving target identification [25]. Prior to this work, polarimetry has been combined with sparsely sampled 3D SAR approaches, with meaningful polarimetric scatterer information being obtained using 3D SAR compressive sensing (CS) [26]. Although useful, this approach also uses the expensive signal reconstruction processes associated with single-channel compressive sensing. Recent publications have improved the scatterer identification of the polarimetric 3D CS-based approach, employing mixed-regularisation reconstruction methods and novel polarimetric decompositions [27, 28]. The polarimetric decompositions used in these approaches, however, are not directly applicable to the multistatic geometries used in this study.

The most established sparse polarimetric 3D SAR technique is polarimetric SAR interferometry [29]. This technique uses the phase unwrapping process utilised by conventional SAR interferometry. The polarimetric diversity is used to optimise the coherence between SAR passes, which leads to smaller phase ambiguities and more accurate scatterer height estimates [30]. Recent publications have exploited this for 3D interferometric inverse-SAR (InISAR) image formation, forming complex point cloud models of a full-size model tank [31–33]. Like the PolSSARVI algorithm, these publications do not use phase unwrapping for complex targets. These studies found that the use of multiple polarisations was able to produce more accurate and stable point cloud models for a complex target, leading to improved target identification. Although the algorithms in these publications are different to the one presented in this paper, they show that performance gains are possible when using multi-polarimetric data.

The detection performance of PolSSARVI, for a range of sub-Nyquist sampled apertures, will be compared to the non-polarimetric SSARVI approach previously presented, using both simulated and experimental data. It will also be shown that PolSSARVI provides accurate polarimetric information, associated with sub-Nyquist-formed 3D renderings of targets. The extraction of bistatic polarimetric parameters used in this study has been previously validated at the Cranfield GBSAR laboratory, using finely sampled SAR collection geometries [6].

Section 4 presents simulation results. Section 5 describes the Cranfield GBSAR laboratory. Section 6 outlines the experimental procedure and polarimetric features of the model target. Section 7 compares the PolSSARVI algorithm to the SSARVI algorithm and assesses the accuracy of polarimetric data obtained with the PolSSARVI algorithm, followed by a discussion. Concluding remarks are provided in Section 8.

2 | Development of the PolSSARVI Algorithm

The SSARVI algorithm described in previous work [18, 19] uses a set of volumetric interferograms that are formed for a single polarisation, using N sparsely and unevenly distributed in height SAR passes. To be more specific, for the case of multistatic collections, the passes as described by their bistatic equivalent monostatic (BEM) trajectories, should be sparsely and unevenly distributed in height. For a given scene centre, a BEM antenna position is defined along the bisecting line (bisectrix) of the transmitter and receiver positions relative to the scene centre and at the bistatic range from the scene centre. N-1 volumetric interferograms are formed using a common reference image, and the phase factors of each interferogram are summed as follows:

$$R(\boldsymbol{x}) = \frac{1}{N}\left|1 + \sum_{n=1}^{N-1} e^{i\varphi_n(\boldsymbol{x})}\right| \tag{1}$$

where $\varphi_n(\boldsymbol{x})$ is the phase at image voxel $\boldsymbol{x}$ of the nth interferogram. Voxels, with a value of R, surpassing a threshold, are classed as a 3D scatterer detection location. This approach utilises volumetric processing when forming a set of sparsely sampled interferograms, which removes the need to account for the layover distortions when summing the interferograms [34]. A consistent elevation angle across the imaged scene is not required for this approach, which also allows for bistatic, multistatic and SAR near-field geometries to be processed more easily.

However, a weakness of this SSARVI approach is that it acts only on single polarimetric channels at a time—it may, for example, be the case that some objects spread their scattering response over several polarimetric channels. In this case it would be advantageous to detect these responses in a joint manner, helping to raise a joint polarimetric phase factor sum R above the scatterer detection threshold.

For the generalised polarimetric algorithm, termed PolSSARVI, data are again collected from N sparsely sampled and unevenly distributed in height SAR passes, though now for all four polarisation channels (in the linear basis: HH, HV, VH and VV). Firstly, for a given pass n, across each set of four polarisations labelled p, the four complex values at a given SAR image voxel, $a_{np}(\boldsymbol{x})$, can be regarded as a two-by-two polarimetric scattering matrix (with four elements labelled p), whose polarimetric span is given by Equation (2)

$$S_n(\boldsymbol{x}) = \sum_{p=1}^{4} \left|a_{np}(\boldsymbol{x})\right|^2 \tag{2}$$

The nth span-normalised polarimetric interferogram for polarisation p is here defined in Equation (3):

$$\Gamma_{np}(\boldsymbol{x}) = \frac{a_{np}(\boldsymbol{x})a^*_{N\,p}(\boldsymbol{x})}{\sqrt{S_n(\boldsymbol{x})S_N(\boldsymbol{x})}} \tag{3}$$

where without loss of generality, pass N is chosen to be the reference pass. Note that with this definition, the magnitude of each polarimetric interferogram is generally not equal to one.

Now, we define the sum over all the interferograms for a given polarisation in Equation (4):

$$\beta_p(\boldsymbol{x}) = \frac{1}{N}\sum_{n=1}^{N} \Gamma_{np}(\boldsymbol{x}) \tag{4}$$

Finally, we may now define the generalised polarimetric phase factor sum, to be used for scatterer detections, as follows:

$$R_{\text{pol}}(\boldsymbol{x}) = S_N(\boldsymbol{x}) \sum_{p=1}^{4} \frac{\left|\beta_p(\boldsymbol{x})\right|^2}{\left|a_{Np}(\boldsymbol{x})\right|^2} \tag{5}$$

It is the case that $R_{\text{pol}} \leq 1$, and thus a threshold value less than one, to be determined, is applied for scatterer detections.

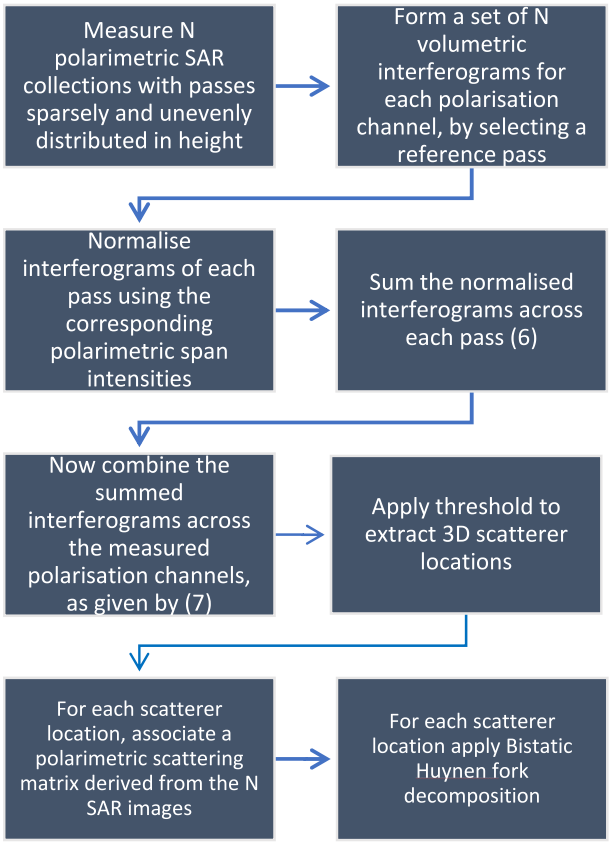

FIGURE 1 | Flow diagram outlining the PolSSARVI algorithm.

For each detection and for each of the four polarisations, the mean SAR image complex pixel value may be obtained $^1/_N\sum_{n=1}^{N} a_{np}(\boldsymbol{x})$, providing what can be regarded as a two-by-two polarimetric scattering matrix (with four elements, labelled as p). Thus, for each of these detections, the bistatic Huynen fork parameters, or any other polarimetric decomposition, can be determined. The whole PolSSARVI process is described in the flow diagram in Figure 1.

It is noted that alternative phase factor sum expressions are possible, giving varying levels of detection performance. In particular, one may define a generalised polarimetric phase factor sum term which has its form in correspondence with (1).

$$R_{\text{pol2}}(\boldsymbol{x}) = \left|\sum_{p=1}^{4} \beta_p(\boldsymbol{x})\right| = \frac{1}{N}\left|1 + \sum_{p=1}^{4}\sum_{n=1}^{N-1} \Gamma_{np}(\boldsymbol{x})\right| \tag{6}$$

However, the detection performance for R_{pol2} has been found to be no better, and sometimes worse, than that for R_{pol} in (5), likely due to sensitivity and complex summation over polarisation terms.

3 | Bistatic Polarimetry & Huynen Fork Parameters

Bistatic radar polarimetry has seen a significant degree of interest from the 1990s onwards [35, 36]. Bistatic polarimetry is generally more complicated than monostatic, as cross-

polarisation terms are no longer equivalent. In this paper, we employ a robust bistatic polarimetric decomposition developed by Titin-Schnaider which builds on the work by Huynen [22–24]. Huynen showed that the scattering matrix of a target illuminated monostatically, $\underline{S}$, can be written in the diagonalised form given by equation (7):

$$\underline{S} = \underline{U}(\Theta, \tau)^{*} \underline{S_d}(\gamma, \nu) \underline{U}(\Theta, \tau)^{\dagger} \tag{7}$$

where the superscript '*' represents the complex conjugate, '†' represents the complex conjugate transposed and the underline represents a matrix quantity. Θ, τ, γ and ν are the four real-independent Huynen fork parameters describing polarimetric properties of the scatterer; $\underline{U}$ is a unitary matrix constructed for the diagonalisation of $\underline{S}$; $\underline{S_d}$ is a diagonalised matrix that contains information about the polarisability of the scatterer and nominally about whether the number of reflections associated with the scattered ray is odd or even [21].

Titin-Schnaider showed that the Huynen diagonalisation approach could be extended to the bistatic case, as presented in Equation (8):

$$\underline{S} = \underline{U}(\Theta_i, \tau_i)^{*} \underline{S_d}(\gamma, \nu) \underline{V}(\Theta_s, \tau_s)^{\dagger} \tag{8}$$

where θ_i, τ_i, θ_s and τ_s are redefined to include the orientation and symmetry of the scatterer for incident "i" and "s" scattered wave directions; and $\underline{U}$ and $\underline{V}$ are unitary matrices which diagonalise the asymmetric scattering matrix for bistatic radar geometries. The approach developed by Titin-Schnaider was further developed by Xu et. al. [37], presenting a computationally efficient algorithm.

The Huynen fork parameters are summarised as follows:

- Orientation/Tilt angle, θ: The angle of the dipole type scattering orientation to the horizontal plane about the line from the transceiver to the scatterer, in the anticlockwise direction, when looking down-range. The range of definition is $-90° \leq \theta \leq 90°$. In the monostatic case, there is one orientation parameter; however, in the bistatic case, this is replaced by two: θ_i denoting the incident direction orientation relating to the transmitter and θ_s denoting the scattered direction orientation relating to the receiver;
- Symmetry angle, τ: A parameter indicating how symmetric a scatterer is about the orientation direction. The range of definition is $0° \leq |\tau| \leq 45°$ where 0° indicates high symmetry and $|\tau| = 45°$ indicates low symmetry. In the monostatic case, there is only one symmetry parameter; however, in the bistatic case, this is replaced by two: τ_i denoting the incident direction symmetry relating to the transmitter and τ_s denoting the scattered direction symmetry relating to the receiver;
- Skip angle, ν: A parameter indicating whether the scattered ray has had an odd or even number of interactions (bounces) with the target. The range of definition is $0° \leq |\nu| \leq 45°$ where 0° indicates an odd-bounce interaction and $|\nu| = 45°$ indicates an even-bounce interaction. Odd-bounce type scatterers include spheres, flat plates and trihedral multi-bounce. Even-bounce scatterers include dihedral multi-bounce;
- Polarisability angle, γ: A parameter indicating how polarising a scatterer is—a measure of how much the incident polarisation is projected on to any particular orientation. The range of definition is $0° \leq \gamma \leq 45°$ where 0° indicates high polarisability and 45° low. Scatterers with medium to high polarisability include rods and the straight edges of extended objects. Scatterers with low polarisability include spheres, flat plates and corner reflectors with multi-bounce, including both dihedrals and trihedrals.

The six Huynen parameters extracted for the experimental work of this paper were obtained via singular value decomposition [37], with the main experimental point-cloud renderings being presented for the rotationally independent parameters ν and γ.

4 | Simulations

Simulations were conducted to verify the effectiveness of the PolSSARVI approach and compare its combined interferometric response to the response of the more basic SSARVI approach across multiple polarisation channels. Simulations were performed on isotropic point scatterers and used a sparsely sampled 2D bistatic SAR aperture, as seen in Figure 2. For simplicity, scatterers were given the *monostatic* polarimetric response of a flat plate, a dihedral and of dipole scatterers. The antennae geometry and scatterer locations of the first simulation are shown in Figure 2.

The vertical extent of the transmitter aperture is 1.74 m, with a mean pass separation of 2° in elevation to the scene centre at the origin. The mean bistatic angle was 14.4°. This is the angle between the mid-transmitter aperture point and the receiver location through the scene centre. Using a frequency range of 7–8 GHz, this would give a theoretical unambiguous vertical cross-range extent of 1.11 m. The unambiguous extent is approximately equal to half of the 2-m vertical target extent. The point scatterers were situated between 9.5 and 10.5 m in a ground range from the transmitter aperture. The dihedral and dipole scatterers were orientated, respectively, at 22.5° and 45° anticlockwise to the down-range direction, so that in the form of a

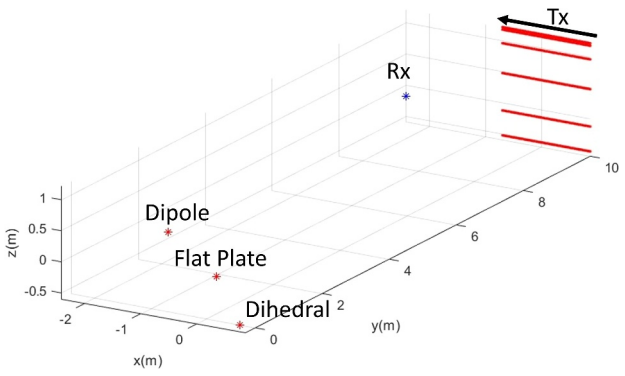

FIGURE 2 | Sparse bistatic SAR simulation geometry. The transmitter aperture (red) is labelled as Tx and receiver position is as labelled Rx. The flat plate, dihedral and dipole scatterers are labelled in the scene.

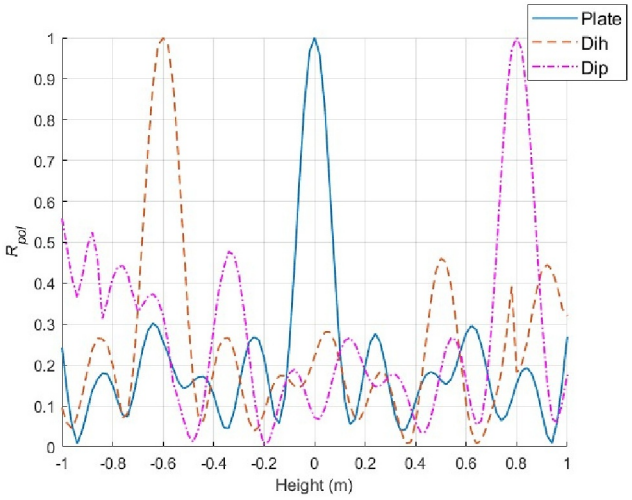

FIGURE 3 | Summed interferometric response R_{pol} along vertical iso-range arcs through the location of the flat plate, dihedral and dipole scatterer. These are labelled as Plate, Dih and Dip, respectively.

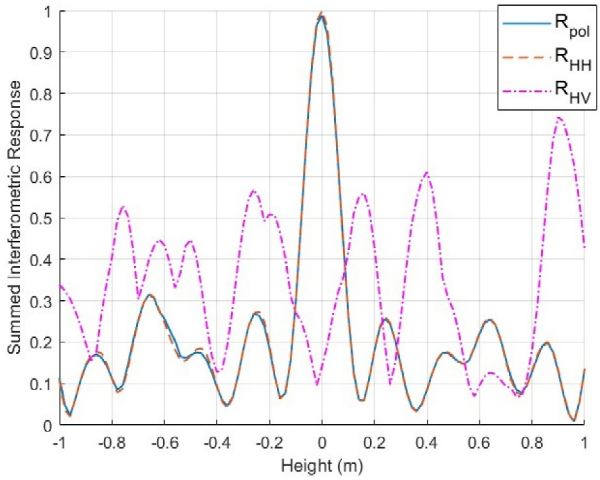

FIGURE 4 | Summed interferometric responses along the vertical iso-range arc through the location of a horizontal dipole. The PolSSARVI response R_{pol} and the SSARVI response R_{HH} appear overlaid.

two-by-two scattering matrix, their polarimetric responses in the linear polarimetric basis were set as presented in (9):

$$\begin{aligned} \underline{S}_{\text{plate}} &= \frac{1}{\sqrt{2}}\begin{bmatrix} 1 & 0 \\ 0 & 1 \end{bmatrix} \\ \underline{S}_{\text{dih}}(22.5°) &= \frac{1}{2}\begin{bmatrix} 1 & 1 \\ 1 & -1 \end{bmatrix} \\ \underline{S}_{\text{dip}}(45°) &= \frac{1}{2}\begin{bmatrix} 1 & 1 \\ 1 & 1 \end{bmatrix} \\ \text{where, } \underline{S} &= \begin{bmatrix} HH & HV \\ VH & VV \end{bmatrix} \end{aligned} \tag{9}$$

Figure 3 presents the summed interferometric response R_{pol} along vertical iso-ranges (constant range) arcs through the three scatterers.

The R_{pol} curves attain maximum values of 1 when passing through their respective scatterers at the correct heights of −0.6 m, 0 and 0.8 m. The R_{pol} curves have low sidelobes. Using conventional image formation algorithms, with a transmitter aperture sampled evenly in elevation, would result in aliased peaks which would significantly increase scatterer height ambiguity and result in false detections.

To contrast the performance of the new PolSSARVI algorithm in comparison to the SARVI algorithm, an additional simulation is run, using the previous bistatic SAR geometry of Figure 2, though with only a single scatterer, consisting of a horizontal dipole at 0 m height. A low level of noise is added to each polarimetric channel to illustrate algorithm behaviour where scatterer polarimetric responses are very low. In the channels with the signal present, the signal to noise ratio (SNR) was 60 dB.

In Figure 4, vertical iso-range plots for R_{pol} (PolSSARVI) and the SSARVI-derived R for the single HH and HV polarimetric channels are presented.

Dipoles are polarising scatterers, showing a strong response in a single polarisation orientation, and in this case, the strong response is in the HH channel only. The combined polarisation PolSSARVI approach provides a clear and correctly located peak. The SSARVI approach also provides a correct detection in the HH channel (R_{pol} and R_{HH} appear overlaid); however, in the HV channel, as expected, the scatterer is not correctly detected. The highest peak in R_{HV} is in the wrong location so that the SSARVI threshold application step would lead to an erroneous detection.

The performance of the PolSSARVI approach has been found to be invariant to the polarimetric scatterer type and orientation, whereas the application of the SSARVI approach on individual polarisations followed by a combination of the detections leads to false detections when scatterers show a dim response in any given polarimetric channel.

5 | Cranfield GBSAR Laboratory Overview

5.1 | Experimental Setup

The SSARVI and PolSSARVI algorithms were applied to an experimental multistatic SAR dataset, collected at the Cranfield GBSAR laboratory. The laboratory contains a representative target scene, with the quarter-scale model tank situated on a gravel ground surface, as shown in Figure 5. The model tank target is approximately 80 cm in height and 2.5 m in length. The gravel scene is approximately 3.5 m in width and 4.5 m in length and is marked by the sphere reflectors shown around the edges. A large reference sphere towards the back of the target scene is visible in Figure 5 and is elevated slightly off the ground. The phase-history data were recorded using a keysight vector network analyser (VNA), which is also linked to the two antennas by high fidelity microwave cables.

The transmitter and receiver are situated on independent antenna rails, each capable of sweeping out 3.5 m in width and 1.9 m in height. Using this setup, a finely sampled 2D multistatic aperture was used as the initial collection geometry,

consisting of 95 vertically spaced horizontal transmitter passes with a 1.5-cm spacing in height, together with two fixed receiver positions to the left of the aperture, as depicted in Figure 6. The collection was fully polarimetric with a frequency range of 6.62–10 GHz.

The transmitter aperture extent was 3.5 m wide and 1.5 m high, providing azimuth and elevation transmitter apertures of 44° and 17.7°. These values were determined relative to the scene centre, which was 4.15 m from the transmitter aperture. The mean bistatic angles to the receiver positions Rx1 and Rx2 were 61.4° and 62.8°, respectively, giving ground-range resolutions of 5.7 and 5.4 cm and cross-range resolutions of 5.5 and 5.4 cm, respectively. The theoretical vertical resolutions for Rx1 and Rx2 were 13.6 and 13.5 cm, respectively. The resolution values were determined from the BEM aperture relative to the scene centre.

FIGURE 5 | Photographs of model tank target. The wire on top is denoted by "W", the turret of tank denoted by "T" and the reference sphere is denoted by "S".

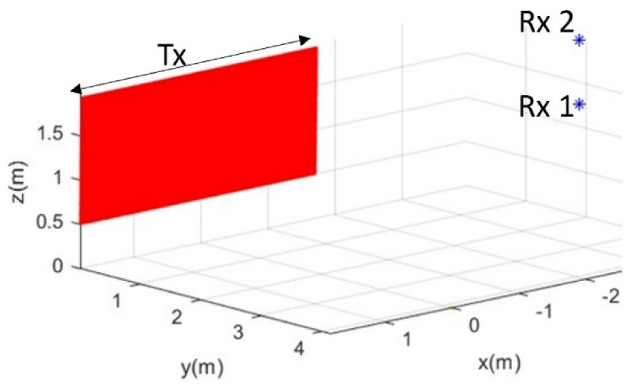

FIGURE 6 | Multistatic SAR geometry. The 2D transmitter SAR aperture is shown in red and denoted by Tx. The stationary receiver positions are shown with blue asterisks and denoted by Rx1 and Rx2.

5.2 | Polarimetric Calibration

Polarimetric calibration is achieved by the measurement of calibration scattering targets with known scattering responses, following Sarabandi et al. [38]. Metal spheres were employed as calibration scatterers since their theoretical scattering matrix can be computed accurately. Additionally, a strong cross-polarisation scatterer was also employed, consisting of a dihedral with vertex rotated to several angles, including 22.5° and 45° to the vertical.

6 | Methodology

6.1 | Aperture Downsampling

For conventional image formation with the laboratory scenario, a minimum transmitter pass spacing height of 7.8 cm in height would be required to suppress aliasing artefacts over a 1.8-m high volume of interest (VoI). This aperture spacing is a subset of the very finely sampled SAR geometry presented in Figure 6 and shall be referred to here as the sub-initial sampling (SIS). However, in accordance with the SSARVI and PolSSARVI requirements, for the downsampling procedure, it was convenient that while maintaining the required average spacing, the SIS had randomized heights. For algorithm evaluation, the transmitter aperture was repeatedly downsampled from the SIS to form sparse 2D apertures, with a mean pass vertical sampling below the minimum Nyquist sampling requirement. This was achieved by removing passes randomly from heights within the transmitter vertical aperture extent. The subsampled transmitter apertures are presented in Figure 7.

The first subsampled geometry, presented in Figure 7, consisted of a mean transmitter pass spacing of 7.8 cm. This is the SIS aperture at the minimum mean spacing required for suppressing artefacts over the VoI around the target. For the range of sparse apertures presented, the performance of the

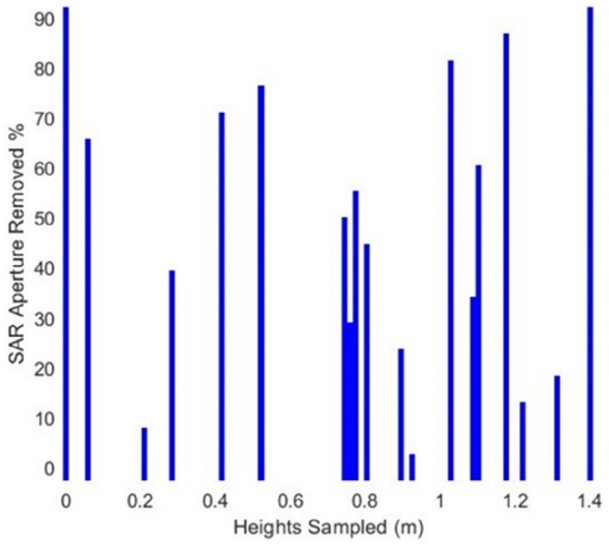

FIGURE 7 | Downsampled transmitter height apertures. Blue lines show heights sampled for a given randomly downsampled aperture. White spaces consist of fully removed SAR passes.

PolSSARVI and SSARVI approaches was compared. The performance was determined by the presence of false scatterer detections and the accuracy of the polarimetric information obtained.

6.2 | Sub-Nyquist Imaging Performance Measures

Numerical measures were used to determine the performance of the PolSSARVI algorithm and compare its performance to the SSARVI algorithm. This was undertaken with sub-Nyquist sampled apertures. The measures included a determination of the level of false detections present in the point clouds, a cross-correlation of sub-Nyquist formed imagery with SIS-formed imagery and a measure of the accuracy of the bistatic Huynen fork parameters.

The level of false detections was determined by measuring the false alarm ratio (FAR) for a range of aperture samplings below the Nyquist sampling. The FAR is given by

$$FAR = \frac{FP}{TP + FP} \tag{10}$$

where FP denotes the number of false positive erroneous detection of artefacts, and TP denotes the number of true positive correct detections [39].

The TP and FP scatterer detections were determined from two 3D binary mask images for the model tank target. To form the masks, two separate span polarisation volumetric images were formed from fully sampled SAR aperture data with the back-projection algorithm (BPA), one for each receiver. The binary mask of each image was formed by applying a span-intensity threshold at 50 dB below the maximum of each image. The TP and FP scatterer locations of each mask image were thus determined and combined into a single dataset.

In addition to the FAR measurements, a further quantitative analysis of the sub-Nyquist aperture performance of the SSARVI and PolSSARVI algorithms was provided by normalised cross-correlation results. The normalised cross-correlation was performed between the 3D point clouds formed with the SIS aperture and the successively downsampled apertures. The polarimetric span intensity was associated for each detection location in the point clouds used in the cross-correlation. This approach, applied to both algorithms, gave a numerical indication of image quality.

The polarimetric properties of the model tank structure were determined by the Huynen parameters. The accuracy of the Huynen parameters obtained for the sub-Nyquist-formed PolSSARVI detections was determined by making a comparison with Huynen parameter arrays obtained from the full SAR aperture BPA images, which will be referred to as Huynen reference arrays. The BPA-formed Huynen parameters obtained for the model tank target were validated in the previous work [19].

For a quantitative comparison, the normalised mean squared deviation (NMSD) was employed for any given Huynen parameter:

$$\overline{\sigma}^2 = \frac{\sum_{i=1}^{D_j} |F(\boldsymbol{x_i}) - F_{\mathrm{RA}}(\boldsymbol{x_i})|^2}{D_i\, G^2} \tag{11}$$

where i enumerates detections of which there are D_j in total for the jth sparse aperture; $F(\boldsymbol{x_i})$ is the value of a particular Huynen parameter for detection i at location $\boldsymbol{x_i}$; $\mathrm{F_{RA}}(\boldsymbol{x_i})$ is the corresponding value of the same Huynen parameter reference array; and G is the range of the specific Huynen parameter. Measurements of the NMSD are supplemented by the maximum intensity projections (MIPs) of the model tank target presented in Section 7.3. The Huynen parameters determined for each SIS aperture size are presented at each projected voxel location.

It is noted that there were slight variations in the location of scatterer detections for the different aperture samplings; however, the NMSD results in Section 7.3 were restricted to evaluation over 'TP' detections only, which reduced the variations.

6.3 | Huynen Reference Array

The Huynen parameters were determined for full SAR aperture BPA images from each receiver separately. For each Huynen parameter and image position, the mean values over the two receiver antennas were used to form the Huynen parameter reference arrays used in Equation (11). The Huynen reference

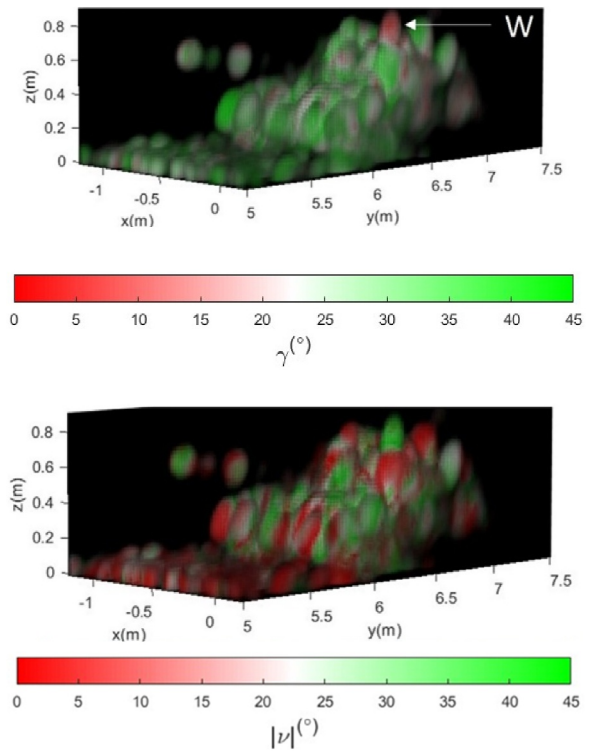

FIGURE 8 | Multistatic 3D BPA SAR images of the model vehicle, formed with the full transmitter aperture presented in Figure 6. Polarimetric span-intensity in dB provides the brightness in these images, and colour is attributed to polarimetric parameter angles. The polarisability angle is shown (top) together with the skip angle (bottom). "W", in the top rendering, denotes the position of the wire, which is seen to have a high polarisability value.

arrays were used to colour the span polarisation BPA SAR images presented in Figure 8 (formed with full SAR apertures). VoxView software [40] was used to form the 3D renderings, where both the brightness and the opacity of each voxel are determined by the polarimetric span-intensity. The polarimetric span-intensity is presented with a dB scale, with a dynamic range of 50 dB. The figure shows renderings for both the polarisability angle and the skip angle.

The top rendering shows the polarisability angle across the tank scene. Nonpolarising scatterers appear as green and polarising scatterers as red. The tank structure is seen as mainly nonpolarising, except for the wire labelled as 'W' on the top of the tank. The bottom rendering shows the skip angle across the tank scene, with red indicating an odd-bounce response and green indicating an even-bounce response. A mixture between odd and even bounce scattering mechanisms is seen to be present across the tank structure, which may be expected due to the complex nature of the target. The reference sphere at the back of the scene allowed a validation check on the polarimetry: It was seen to show the expected strong single/odd-bounce and nonpolarising scattering.

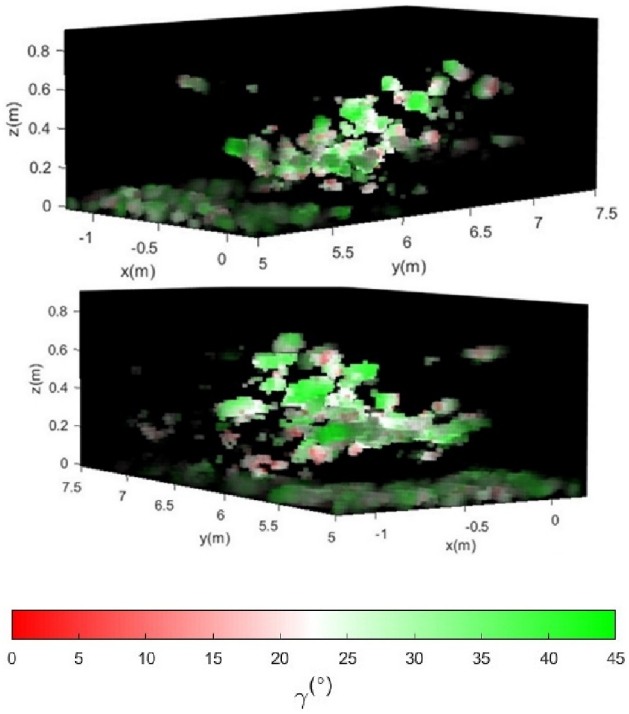

FIGURE 9 | Sub-Nyquist SAR aperture polarimetric and multistatic T72 rendering showing the Huynen polarisability angle. Green shows nonpolarising scatterers, and red shows polarising scatterers. Two different viewing angles of the same rendering are shown.

7 | Results and Discussion

7.1 | Sub-Nyquist Point Clouds

The SSARVI and PolSSARVI thresholding values used (see Figure 1) are described numerically by Equation (12):

$$T = \alpha(max(R) - \text{mode}(R)) + \text{mode}(R) \tag{12}$$

where α is referred to here as the threshold factor where $0 \leq \alpha \leq 1$, and was varied to determine an optimal threshold T. The modal values of the interferometric phase factor sum R were determined for both SSARVI and PolSSARVI approaches [41].

The threshold factor was determined by sequentially increasing its value on finely sampled experimental imagery until the background noise and sidelobe artefacts were no longer visible in the point clouds. For the PolSSARVI algorithm, there were no visible background erroneous detections above $\alpha = 0.5$. For the SSARVI algorithm, there were no visible background artefacts above $\alpha = 0.75$. These values of α were adopted for subsequent point cloud generation.

Example renderings of the PolSSARVI algorithm being used to form sub-Nyquist sampled multistatic polarimetric 3D pointclouds are presented in Figure 9. The polarisability angle is represented through colour. Two different orientations are presented, the top one with the tank barrel pointing left and the bottom one pointing right. The renderings were produced using VoxView, as was the case for Figure 8.

Figure 9 was formed using a sparse multistatic geometry, using 57% aperture removed from SIS (ARF-SIS) with a mean spacing of 18.1 cm. The two stationary receiver locations that were shown in Figure 6 were used to form the imagery. The thresholding was applied to the data from each receiver separately, with the detection points from each then overlaid. No false scatterer detections are present.

As was the case in the BPA rendering, the result shows a predominantly nonpolarising scattering response for the PolSSARVI point cloud, though a small number of polarising scatterers can be seen. The wire, visible in Figure 8a, was not visible in the PolSSARVI rendering.

In correspondence with Figures 9, Figure 10 shows the Huynen skip angle determined at each point in the point cloud rendering, formed from a 57% ARF-SIS aperture.

The main tank structure shows a mixture of odd-bounce and even-bounce scatterings, as was the case for the full aperture BPA rendering in Figure 8. The cannon shows a similar response to the corresponding locations in the full aperture BPA image. The reference sphere at the back of the scene correctly showed a distinct odd-bounce scattering response for all aperture samplings.

7.2 | Sub-Nyquist Performance of SSARVI and PolSSARVI Algorithms

The false alarm ratio (FAR) was determined for PolSSARVI and SSARVI algorithms, using a multistatic dataset that was sub-Nyquist sampled in elevation. The apertures used to measure the FAR were presented in Figure 7 and were formed by sequentially downsampling the SIS aperture, as described in Section 6.1.

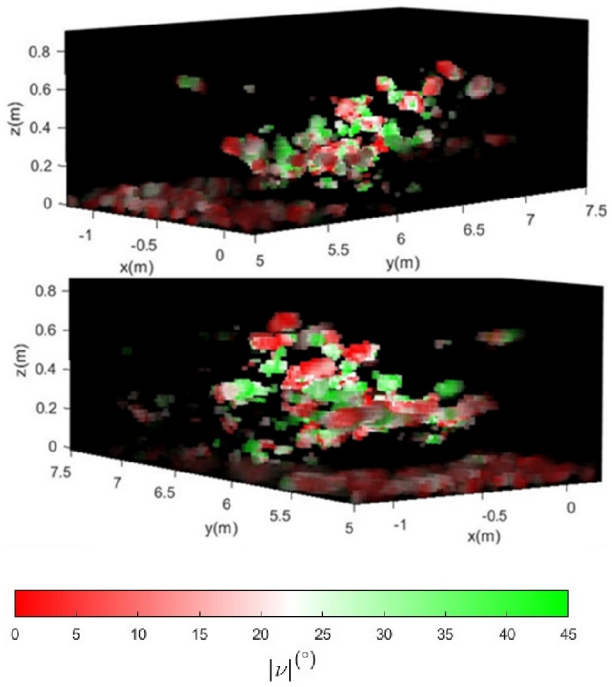

FIGURE 10 | Sub-Nyquist SAR aperture polarimetric and multistatic T72 rendering showing the Huynen skip angle. Green shows even-bounce scatterers, and red shows odd-bounce scatterers. Two different viewing angles of the same rendering are shown.

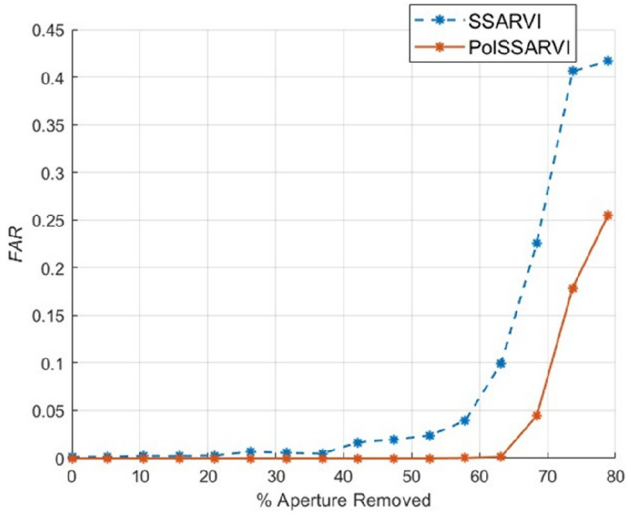

FIGURE 11 | False alarm ratio (FAR) of the SSARVI and PolSSARVI approaches for sub-Nyquist SAR aperture samplings below SIS.

Figure 11 compares the FAR of the SSARVI and PolSSARVI approaches. The FAR measured at each aperture sampling is given by Equation (10). The 'TP' and 'FP' scatterer locations were determined from the corresponding mask images as described in Section 6.2.

As the transmitter aperture was downsampled from 0% to 37% ARF-SIS, the SSARVI approach showed a negligible FAR. At 42% ARF-SIS, the erroneous artefact detections became more visible around the target and the measured FAR started to increase. The level of artefact detections started to have a significant presence on the rendering at 57% ARF-SIS, at which point the FAR started to increase at a sharper rate and the tank structure was difficult to discern. At 63% aperture removal below SIS, the tank structure became indiscernible from artefact detections, at which point the measured FAR was approximately 0.1.

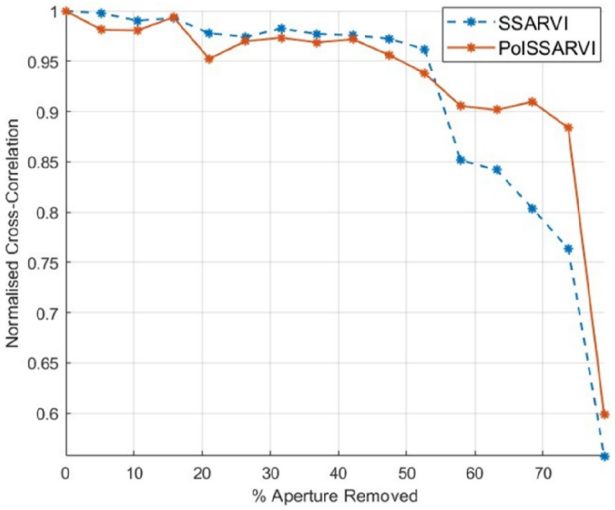

FIGURE 12 | Normalised cross-correlation of sub-Nyquist-formed point clouds with the initial SIS point cloud, performed for both SSARVI and PolSSARVI algorithms.

For the PolSSARVI approach, there were no visible artefact detections up to 57% ARF-SIS. At 63% ARF-SIS, there was a minor level of erroneous detections, with a negligible effect on the FAR. The FAR started to increase significantly at 68% ARF-SIS. The tank structure became indiscernible from erroneous detections at 73% ARF-SIS, with a FAR of approximately 0.17.

Comparing the two approaches, the PolSSARVI algorithm showed fewer erroneous detections over a larger range of aperture samplings below Nyquist sampling. The tank structure also became indiscernible at a lower aperture sampling, compared to the SSARVI algorithm. This implies that it provides an improved performance, with lower aperture sampling requirements.

The FAR was found useful for indicating the presence of artefacts, with values below about 0.1 providing scatterer point clouds with some utility and below about 0.01 providing point clouds of a good quality.

The FAR measurements are supplemented by the normalised cross-correlation results between the sub-Nyquist aperture point clouds and the finely sampled aperture point clouds for both algorithms, as shown in Figure 12 below.

The sub-Nyquist sampled aperture point clouds formed with the SSARVI algorithm show an initial high cross-correlation with the corresponding SIS aperture point cloud. This continues until 47% ARF-SIS, after which the measured cross-correlation starts to noticeably decline. The cross-correlation decreases to 0.85 at 57% ARF-SIS which is noted as being the aperture sampling at which the discernibility of the tank becomes limited due to the

presence of artefact detections. The measured cross-correlation continues to decrease after 63% ARF-SIS, the point at which the tank structure becomes indiscernible.

The measured cross-correlation for the sub-Nyquist aperture point clouds formed of the PolSSARVI algorithm, also shows a high correlation over a similar downsampling range when compared to the SSARVI algorithm. The values obtained for the PolSSARVI algorithm are marginally lower compared to those obtained from the SSARVI algorithm until 52% ARF-SIS. At 57% ARF-SIS, the PolSSARVI algorithm has a higher degree of correlation with the finely sampled point clouds, which is the point at which distinguishability of the tank structure is limited for the SSARVI algorithm. For the PolSSARVI algorithm, only minor artefacts are present at this aperture sampling. The normalised cross-correlation then only shows a significant decrease at 73% ARF-SIS, which is the point at which the tank structure becomes indiscernible from artefact detections.

The high cross-correlation, with the SIS aperture point clouds, for both algorithms until 52% ARF-SIS, suggests they produce high quality imagery. This is for a large range of sub-Nyquist aperture samplings, where the point clouds produced had a high likeness to those formed with finely sampled geometries. The later decline of the cross-correlation for the PolSSARVI algorithm further suggests that a coarser aperture sampling can be used for forming high quality 3D point clouds.

There was a reasonable agreement between the determined FAR at each downsampled aperture and the corresponding measured cross-correlation. The decrease in cross-correlation for the SSARVI algorithm at 57% ARF-SIS corresponded to a sharp increase in the FAR for the same aperture. This was the point at which there was limited discernibility for the tank structure in the SSARVI-formed point clouds and only minor artefacts for the PolSSARVI-formed point clouds. As the cross-correlation for the PolSSARVI algorithm stayed above 0.9 at 57% ARF-SIS, this suggests that 0.9 is a suitable value for obtaining good quality 3D point cloud imagery.

7.3 | Sparsely Sampled Aperture Polarimetry Performance

The validation of the Huynen parameters for sub-Nyquist sampled geometries, using the model tank target, is presented in this section. The NMSD of the Huynen parameters, defined in (11), obtained for the PolSSARVI approach, is shown in Figure 13. They are presented for the sub-Nyquist apertures shown in Figure 7. The NMSD of the Huynen parameters was determined for the sub-Nyquist point-cloud detections across the structure of the target for different aperture samplings.

All the Huynen parameters show the same general trend of maintaining a stable NMSD until about 57% ARF-SIS, after which they go through increases. The curves do have different NMSD levels, however, due to a constant difference between the point cloud detection polarisations and the corresponding BPA-derived Huynen reference arrays (see Section 6.3).

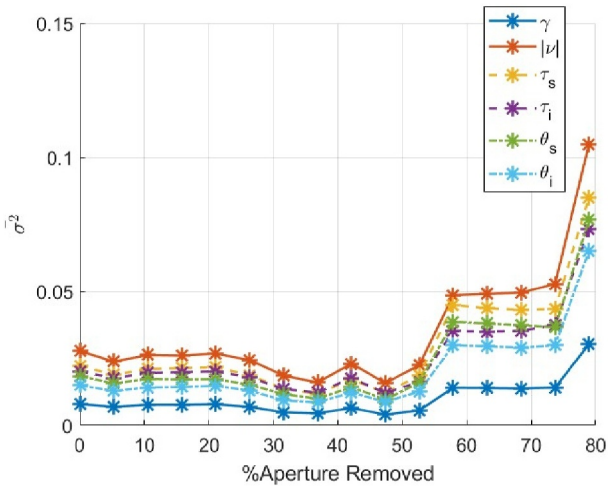

FIGURE 13 | The NMSD of all six bistatic Huynen fork parameters for each aperture sampling.

At 73% ARF-SIS, it is noted that the target structure became indiscernible from erroneous detections, and for more sparse sampling, all the NMSD curves increase further. The polarisability parameter seems to be the least sensitive to aperture downsampling and experienced the least variation in NMSD. This is likely because the scene showed an overwhelmingly nonpolarising scattering response.

Polarimetric point-cloud MIPs are shown in Figures 14–17. The renderings were formed at aperture samplings of 52% ARF-SIS, showing a negligible presence of erroneous detections and a Huynen parameter NMSD below 0.1. The MIPs in Figure 14 provide a front view of the target, showing the maximum polarimetric span in the *y*-direction in a dB scale with a 50-dB dynamic range, with its associated polarisability angle represented by colour.

The top rendering shows the polarisability angle of the tank structure, formed at the SIS aperture. The scattering centre on the turret of the tank, labelled “T”, is the brightest scatterer. Overall, little difference can be seen in the polarisability angle when comparing with the 52% ARF-SIS in the lower figure, confirming the Huynen parameter NMSD results in Figure 13.

Figure 15 presents MIPs formed with the same aperture sampling and polarimetric span-intensity projection as those presented in Figure 14, though the colour here represents the skip angle. Again, there is a good deal of similarity between the images with the different aperture samplings.

Figures 16 and 17 show MIPs corresponding to those in Figures 14 and 15, but now with an *x*-direction projection, providing a side view of the target with the cannon visible, extending beyond the front of the target. Only minor changes in the location of the detections and their polarisation are noticeable between the differently sampled aperture results. The target can be seen to be mostly nonpolarising, and there is some variability in the skip parameter.

Figure 18 shows the Huynen parameters determined at the location of the reference sphere, located to the rear of the target

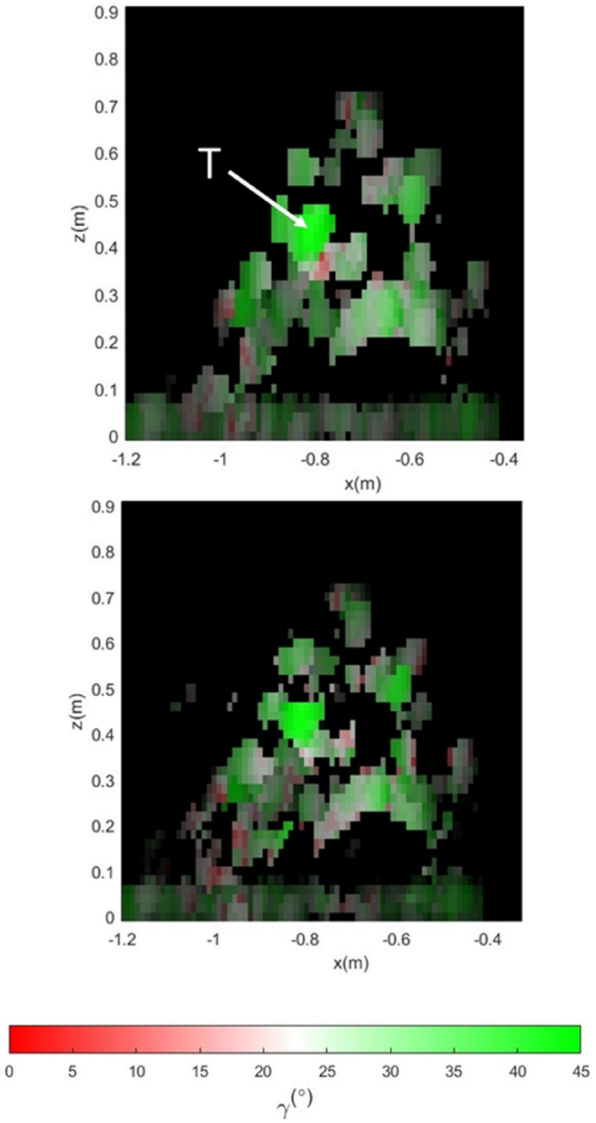

FIGURE 14 | PolSSARVI point-cloud MIPs in the x-z plane, showing a front view of the tank rendering. Colour indicates the polarisability angle, with brightness determined by the polarimetric span in dB, with a 50-dB dynamic range. The renderings were formed at SIS sampling (top) and at 52% ARF-SIS (bottom). The turret is labelled as 'T'.

scene, labelled "S" in Figure 5. These values were extracted for the sparse apertures presented in Figure 7. For all the apertures, the Huynen parameters were measured at a common point on the sphere.

The expected Huynen parameter values for a sphere are 45° for the polarisability angle γ, 0° for the skip angle ν and 0° for the symmetry angles τ_i and τ_s. The orientation parameters Θ_i and Θ_s offer no physical meaning for nonpolarising scatterers [22–24].

The sphere results are in agreement with the expected values, and are stable over the sparse apertures implemented, with the polarisability angle at about 37°, the skip angle at about 1.0° and the sum of the symmetry angles at about 2.7°.

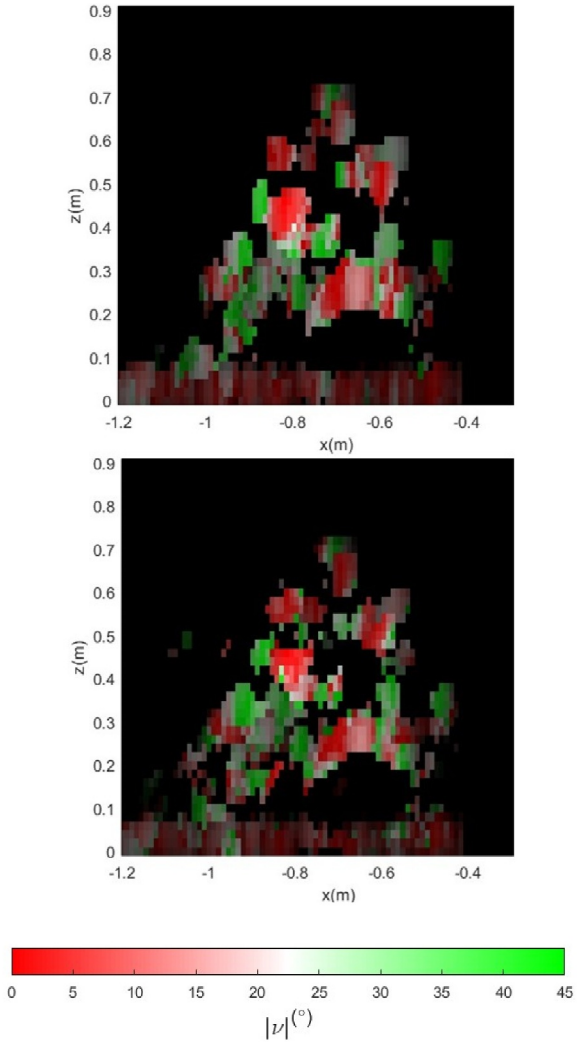

FIGURE 15 | PolSSARVI point-cloud MIPs in the x-z plane, showing a front view of the tank rendering. Colour indicates the skip angle, with brightness determined by the polarimetric span in dB, with a 50-dB dynamic range. The renderings were formed at SIS sampling (top) and at 52% ARF-SIS (bottom).

It is noted that a more substantial validation of Huynen parameter extraction in the GBSAR laboratory was presented in ref. [6] where canonical scatterers including a metal dihedral in different orientations were measured in a monostatic geometry. The use of dihedrals for validation in the current multiple bistatic scenario would have been more difficult, however, given the range of different bistatic geometries used.

7.4 | Discussion

Considering the NMSD results in Figure 13, the stability of the measured Huynen parameters up to 52% ARF-SIS suggests that this is a good minimum aperture sampling for obtaining accurate polarimetric information. This aperture is significantly below the Nyquist sampling requirement and is therefore a large reduction on what would conventionally be required. There was also little observed difference in the point cloud detection locations from 0% to 52% ARF-SIS, which was evidenced in the

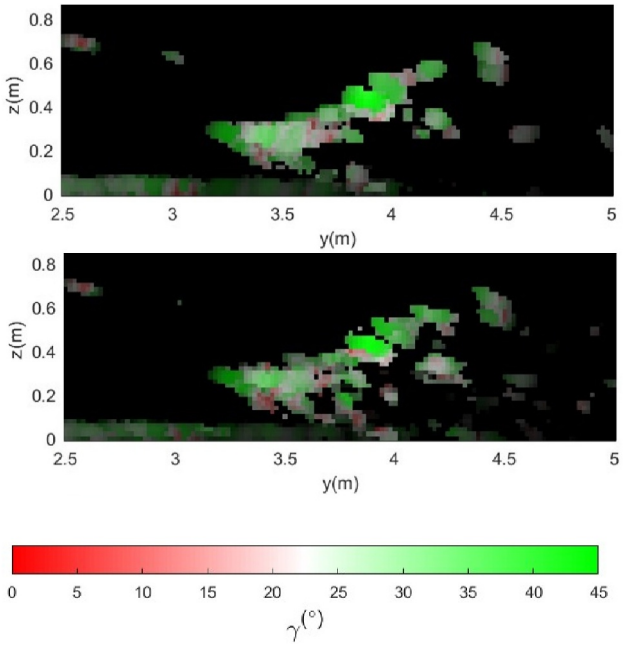

FIGURE 16 | PolSSARVI point-cloud MIPs in the y-z plane, showing a side view of the tank rendering. Colour indicates the polarisability angle, with brightness determined by the polarimetric span in dB, with a 50-dB dynamic range. The renderings were formed at SIS sampling (top) and at 52% ARF-SIS (bottom).

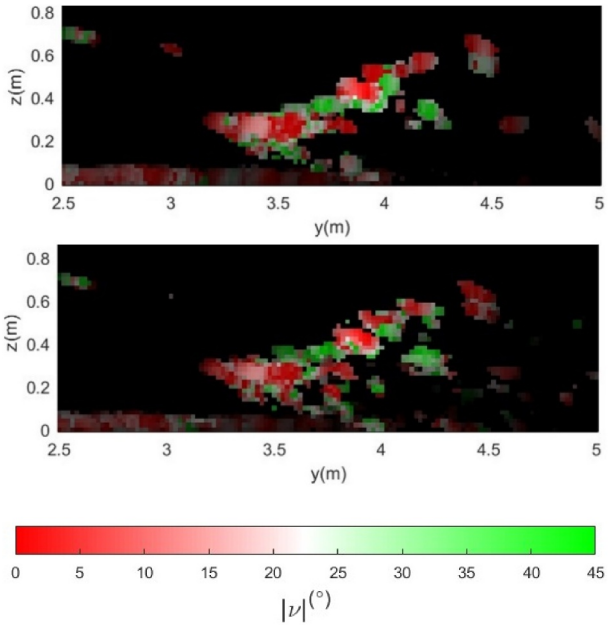

FIGURE 17 | PolSSARVI point-cloud MIPs in the y-z plane, showing a side view of the tank rendering. Colour indicates the skip angle, with brightness determined by the polarimetric span in dB, with a 50-dB dynamic range. The renderings were formed at SIS sampling (top) and at 52% ARF-SIS (bottom).

MIPs presented in Figures 14–17. A negligible FAR was also seen over the same range of sub-Nyquist sampled apertures, as shown in Figure 11.

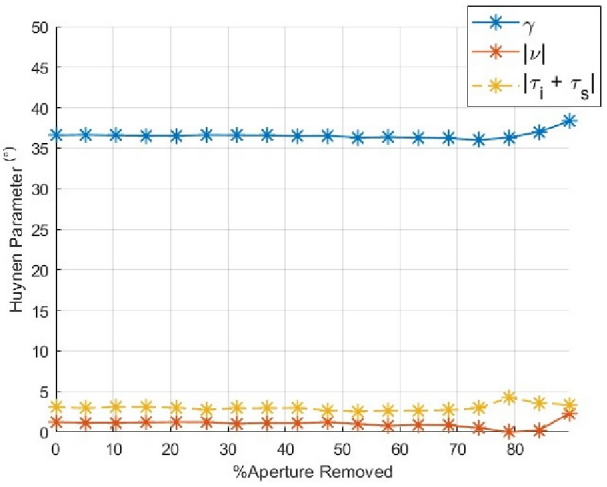

FIGURE 18 | Huynen fork parameters determined at the location of the reference sphere for each aperture sampling.

The tank structure was seen to be largely nonpolarising in both the Huynen reference array and in the various sampled aperture point clouds; so consequently, the polarisability angle showed the smallest NMSD, with the smallest variation. The other Huynen parameters showed a period of stability up to 52% ARF-SIS followed by substantial increases, most strongly seen for the skip parameter. This may be because these parameters, and more so for the skip parameter, had the greatest variability across the target structure, as can be seen in the point-cloud MIPs (e.g., see Figure 17).

There was little variation in the Huynen fork parameters determined on the sphere for all downsampled apertures (see Figure 18). This suggests that the Huynen parameters are most stable for bright and isolated scatterers.

8 | Conclusion

This paper presented and validated the PolSSARVI algorithm, which is a polarimetric extension of the multistatic SSARVI algorithm [18, 19]. Simulations showed that accurate scatterer height locations were determined for polarimetrically diverse scatterers at sub-Nyquist aperture sampling, demonstrated using a near-field bistatic collection geometry.

Simulations showed how the polarimetric combination approach in PolSSARVI reduces false target detections when compared to SSARVI, arising from when scatterers have a relatively dim response in a particular polarisation channel.

With experimental data, it was shown that the PolSSARVI approach had a lower measured FAR compared to the SSARVI approach, where detections from each measured channel were overlaid. For aperture sampling lower than 52% ARF-SIS, the PolSSARVI FAR became significantly lower than that for SSARVI. Furthermore, it was observed that the minimum aperture sampling limit for discerning the target structure was 5% less for the PolSSARVI algorithm than for the SSARVI algorithm.

Both algorithms exhibited a significant initial similarity with the finely sampled point cloud renderings, as evidenced by the normalised cross-correlation measurements presented in Figure 12. The SSARVI algorithm demonstrated a relatively rapid decrease in cross-correlation beginning at 52% ARF-SIS, which coincided with an increase in FAR at the same aperture sampling. In contrast, the PolSSARVI algorithm exhibited a more gradual decline in cross-correlation, indicating that the imagery produced maintains a higher degree of accuracy at the reduced aperture sampling.

The accuracy of the Huynen parameters determined on the sub-Nyquist PolSSARVI-formed point clouds was determined by their NMSD relative to the corresponding values obtained for the Huynen reference arrays formed from BPA full aperture SAR images. A minimal NMSD (lower than 0.03), and low variation in NMSD, was shown across the tank structure down to 52% ARF-SIS apertures, suggesting that this is an optimal minimum aperture size for obtaining accurate polarimetric information. Furthermore, there was little variation in the Huynen fork parameters determined on the sphere for all downsampled apertures, which suggests that the Huynen parameters are most stable for bright and isolated scatterers.

Overall, for the current experimental setup and target measured, it was found that most sparse aperture sampling, which provided negligible FAR, high correlation with finely sampled aperture imagery and accurate Huynen parameter estimations, was 52% ARF-SIS.

For this work, noncoherently overlaying of detections from different bistatic geometries was the method chosen for combing the data from each receiver. The future of this research should therefore focus on assessing different kinds of multistatic receiver data combinations for the PolSSARVI approach, including coherent combination. As with the SSARVI approach, the threshold for the PolSSARVI approach was determined experimentally for the target. It is possible that the threshold for scatterers displaying different polarimetric properties may differ from that observed in this study. In addition to conducting further measurements, thresholds could potentially be derived from electromagnetic simulations of other complex polarimetric targets, and statistical-based methods could also be implemented [16, 42]. The use of CS-related methods, as discussed earlier, could also be incorporated [15, 28]. Alternative polarimetric phase factor summation methods, such as that given by Equation (6), could also be investigated further.

Author Contributions

Richard Welsh: conceptualisation, data curation, formal analysis, investigation, methodology, software, validation, visualisation, writing – original draft, writing – review and editing. **Daniel Andre:** conceptualisation, data curation, formal analysis, funding acquisition, investigation, methodology, project administration, software, supervision, validation, visualisation, writing – review and editing. **Mark Finnis:** resources, software.

Acknowledgements

This investigation was sponsored by Dstl.

Conflicts of Interest

The authors declare no conflicts of interest.

Data Availability Statement

Radar trajectory coordinates will be made available on the CORD repository. Synthetic aperture radar data are the subject of ongoing research but may be made available on request to the corresponding author or the Cranfield GBSAR group.

References

1. C. Hu, Z. Chen, X. Dong, and C. Cui, "Multistatic Geosynchronous Sar Resolution Analysis and Grating Lobe Suppression Based on Array Spatial Ambiguity Function," *IEEE Transactions on Geoscience and Remote Sensing* 58, no. 9 (2020): 6020–6038, https://doi.org/10.1109/tgrs.2020.2969573.

2. F. Santi, M. Bucciarelli, D. Pastina, M. Antoniou, and M. Cherniakov, "Spatial Resolution Improvement in GNSS-Based SAR Using Multistatic Acquisitions and Feature Extraction," *IEEE Transactions on Geoscience and Remote Sensing* 54, no. 10 (2016): 6217–6231, https://doi.org/10.1109/tgrs.2016.2583784.

3. H. Kuang, J. Chen, W. Yang, W. Liu, and X. Zhu, "Fully Three-Dimensional UAV SAR Imaging with Multi-azimuth-angle Observation," in *2017 IEEE International Geoscience and Remote Sensing Symposium (IGARSS)* (IEEE, 2017), 470–473, https://doi.org/10.1109/igarss.2017.8126994.

4. S. Tebaldini, M. Manzoni, L. Ferro-Famil, F. Banda, and D. Giudici, "FDM MIMO Spaceborne SAR Tomography by Minimum Redundancy Wavenumber Illumination," *IEEE Transactions on Geoscience and Remote Sensing* 62 (2024): 1–19, https://doi.org/10.1109/tgrs.2024.3371267.

5. B. Hawkins, M. Anderson, S. Prager, S. J. Chung, and M. Lavalle, "Experiments With Small UAS to Support SAR Tomographic Mission Formulation," in *2021 IEEE International Geoscience and Remote Sensing Symposium (IGARSS)* (IEEE, 2021), 643–646.

6. D. Andre, R. Sabiers, and M. Finnis, "Through-Wall Multistatic Polarimetric 3D SAR," *NATO STO Review* 2022: 1–12: STO-MP-SET 273.

7. J. Elgy, D. Andre, and M. Finnis, "Volumetric SAR Near-Field Upsampling and Basebanding," *Electronics Letters* 56, no. 12 (2020): 622–624, https://doi.org/10.1049/el.2019.4123.

8. C. D. Austin, E. Ertin, and R. L. Moses, "Sparse Signal Methods for 3-D Radar Imaging," *IEEE Journal on Selected Topics in Signal Processing* 5, no. 3 (2011): 408–423, https://doi.org/10.1109/jstsp.2010.2090128.

9. X. X. Zhu and R. Bamler, "Superresolving SAR Tomography for Multidimensional Imaging of Urban Areas: Compressive Sensing-Based TomoSAR Inversion," *IEEE Signal Processing Magazine* 31, no. 4 (2014): 51–58, https://doi.org/10.1109/msp.2014.2312098.

10. R. Carande and D. Cohen, "SAR Point Cloud Generation System," *U. S. Patent Office, WO/2014/074631* (2014).

11. C. Rambour, A. Budillon, A. C. Johnsy, L. Denis, F. Tupin, and G. Schirinzi, "From Interferometric to Tomographic SAR: A Review of Synthetic Aperture Radar Tomography-Processing Techniques for Scatterer Unmixing in Urban Areas," *IEEE Geosci Remote Sens Mag* 8, no. 2 (2020): 6–29, https://doi.org/10.1109/mgrs.2019.2957215.

12. A. Moreira, P. Prats-Iraola, M. Younis, G. Krieger, I. Hajnsek, and K. P. Papathanassiou, "A Tutorial on Synthetic Aperture Radar," *IEEE Geosci Remote Sens Mag* 1, no. 1 (2013): 6–43, https://doi.org/10.1109/mgrs.2013.2248301.

13. H. Tian, C. Dong, H. Yin, and L. Yuan, "Airborne Sparse Flight Array SAR 3D Imaging Based on Compressed Sensing in Frequency Domain," *Journal of Systems Engineering and Electronics* 34, no. 1 (2022): 56–67, https://doi.org/10.23919/jsee.2022.000125.

14. G. Xu, B. Zhang, H. Yu, J. Chen, M. Xing, and W. Hong, "Sparse Synthetic Aperture Radar Imaging From Compressed Sensing and Machine Learning: Theories, Applications, and Trends," *IEEE Geoscience and Remote Sensing Magazine* 10, no. 4 (2022): 32–69, https://doi.org/10.1109/mgrs.2022.3218801.

15. M. Wang, S. Wei, R. Shen, Z. Zhou, J. Shi, and X. Zhang, "3D SAR Imaging Method Based on Learned Sparse Prior," *Journal of Radars* 12, no. 1 (2023): 36–52.

16. M. Woollard, D. Blacknell, H. Griffiths, and M. A. Ritchie, "SARCASTIC v2.0—High-Performance SAR Simulation for Next-Generation ATR Systems," *Remote Sensing* 14, no. 11 (2022): 2561, https://doi.org/10.3390/rs14112561.

17. Z. Manzoor, M. T. Al Qaseer, and K. M. Donnell, "Image Distortion Characterization Due to Equivalent Monostatic Approximation in Near-Field Bistatic SAR Imaging," *IEEE Transactions on Instrumentation and Measurement* 69, no. 7 (2020): 4898–4907, https://doi.org/10.1109/tim.2019.2957868.

18. R. Welsh, D. Andre, and M. Finnis, "Volumetric Interferometry for Sparse 3D Synthetic Aperture Radar With Bistatic Geometries," *Electronics Letters* 59, no. 12 (2023): e12851, https://doi.org/10.1049/ell2.12851.

19. R. Welsh, D. Andre, and M. Finnis, "Laboratory Multistatic 3D SAR With Polarimetry and Sparse Aperture Sampling," *IET Radar, Sonar & Navigation* 18, no. 1 (2024): 184–197, https://doi.org/10.1049/rsn2.12528.

20. S. W. Chen, M. D. Li, X. C. Cui, and H. L. Li, "Polarimetric Roll-Invariant Features and Applications for Polarimetric Synthetic Aperture Radar Ship Detection: A Comprehensive Summary and Investigation," *IEEE Geoscience and Remote Sensing Magazine* 12, no. 1 (2024): 36–66, https://doi.org/10.1109/mgrs.2023.3328472.

21. J. Huynen, "*Phenomenological Theory of Radar Targets*" (PhD thesis, TU Delft, 1970).

22. C. Titin-Schnaider, "Physical Meaning of Bistatic Polarimetric Parameters," *IEEE Transactions on Geoscience and Remote Sensing* 48, no. 5 (2010): 2349–2356, https://doi.org/10.1109/tgrs.2009.2038063.

23. C. Titin-Schnaider, "Characterization and Recognition of Bistatic Polarimetric Mechanisms," *IEEE Transactions on Geoscience and Remote Sensing* 51, no. 3 (2013): 1755–1774, https://doi.org/10.1109/tgrs.2012.2208118.

24. C. Titin-Schnaider, "Polarimetric Characterization of Bistatic Coherent Mechanisms," *IEEE Transactions on Geoscience and Remote Sensing* 46, no. 5 (2008): 1535–1546, https://doi.org/10.1109/tgrs.2008.916078.

25. J. Wang, S. Quan, S. Xing, Y. Li, H. Wu, and W. Meng, "PSO-Based Fine Polarimetric Decomposition for Ship Scattering Characterization," *ISPRS Journal of Photogrammetry and Remote Sensing* 220 (2025): 18–31, https://doi.org/10.1016/j.isprsjprs.2024.11.015.

26. E. Aguilera, M. Nannini, and A. Reigber, "Multisignal Compressed Sensing for Polarimetric SAR Tomography," *IEEE Geoscience and Remote Sensing Letters* 9, no. 5 (2012): 871–875, https://doi.org/10.1109/lgrs.2012.2185482.

27. S. Demirci and Y. Izumi, "Application of H/α Decomposition to Limited and Dual-Polarimetric 3D SAR Data of Civilian Vehicles," *IEEE Access* 11 (2023): 83589–83602, https://doi.org/10.1109/access.2023.3301619.

28. H. Bi, J. Feng, S. Jin, W. Yang, and W. Xu, "Mixed-Norm Regularization-Based Polarimetric Holographic SAR 3-D Imaging," *IEEE Geoscience and Remote Sensing Letters* 21 (2024): 1–5, https://doi.org/10.1109/lgrs.2024.3353801.

29. S. R. Cloude and K. Papathanassiou, "Polarimetric SAR Interferometry," *IEEE Transactions on Geoscience and Remote Sensing* 36, no. 5 PART 1 (1998): 1551–1565, https://doi.org/10.1109/36.718859.

30. F. Xue, X. Wang, F. Xu, and Y. Wang, "Polarimetric SAR Interferometry: A Tutorial for Analyzing System Parameters," *IEEE Geosci Remote Sens Mag* 8, no. 2 (2020): 83–107, https://doi.org/10.1109/mgrs.2019.2954756.

31. K. Wu and X. Xu, "A Fast ISAR Tomography Technique for Fully Polarimetric 3-D Imaging of Man-Made Targets," *IEEE Transactions on Geoscience and Remote Sensing* 60, (2022): 1–12.

32. A. Kumar, E. Giusti, F. Mancuso, S. Ghio, A. Lupidi, and M. Martorella, "Three-Dimensional Polarimetric InISAR Imaging of Non-cooperative Targets," *IEEE Trans Comput Imaging* 9 (2023): 210–223, https://doi.org/10.1109/tci.2023.3248942.

33. A. Kumar, E. Giusti, and M. Martorella, "Hybrid Polarimetry Inverse Synthetic Aperture Radar," *IET Radar, Sonar & Navigation* 19, no. 1 (2025): e70004, https://doi.org/10.1049/rsn2.70004.

34. D. B. Andre and K. Morrison, "A Volumetric Approach to SAR Interferometry," in *Proceedings of the Institute of Acoustics*, vol. 36 (2014).

35. A.-L. Germond, E. Pottier, and J. Saillard, "Foundation of Bistatic Radar Polarimetry Theory," in *Radar Systems* (RADAR 97, 1997), 833–837.

36. E. Lueneburg and S. R. Cloude, "Bistatic Scattering," in *Wideband Interferometric Sensing and Imaging Polarimetry*, 3120 (SPIE, 1997), 56–68.

37. Z. Xu, X. Ai, F. Zhao, and S. Xiao, "A New Bistatic Huynen Target Parameters Extraction Algorithm: Experimental Validation and Data Analysis," *IEEE Transactions on Antennas and Propagation* 70, no. 10 (2022): 9694–9705, https://doi.org/10.1109/tap.2022.3184548.

38. K. Sarabandi, F. T. Ulaby, and M. A. Tassoudji, "Calibration of Polarimetric Radar Systems With Good Polarization Isolation," *IEEE Transactions on Geoscience and Remote Sensing* 28, no. 1 (1990): 70–75, https://doi.org/10.1109/36.45747.

39. P. J. Roebber, "Visualizing Multiple Measures of Forecast Quality," *Weather and Forecasting* 24, no. 2 (2009): 601–608, https://doi.org/10.1175/2008waf2222159.1.

40. T. Marston, VOXview, accessed September, 2023, https://uk.mathworks.com/matlabcentral/fileexchange/78745-voxview.

41. J. C. Russ and F. B. Neal, *The Image Processing Handbook*. 7th ed. (CRC Press, 2016).

42. C. Zhang, G. Gao, J. Liu, and D. Duan, "Oriented Ship Detection Based on Soft Thresholding and Context Information in SAR Images of Complex Scenes," *IEEE Transactions on Geoscience and Remote Sensing* 62 (2024): 1–15, https://doi.org/10.1109/tgrs.2023.3340891.

Polarimetry for sparse multistatic 3D SAR

Welsh, Richard

2025-01-01

Welsh R, Andre D, Finnis M. (2025) Polarimetry for sparse multistatic 3D SAR. IET Radar, Sonar & Navigation, Volume 19, January/December 2025, Article number e70020
https://doi.org/10.1049/rsn2.70020